nature communications

Article

https://doi.org/10.1038/s41467-025-59208-0

Acidity-driven gas-particle partitioning of nitrate regulates its transport to Arctic through the industrial era

Received: 3 July 2024

Accepted: 14 April 2025

Published online: 19 May 2025

Check for updates

Yoshinori Iizuka[1,11] ✉, Mai Matsumoto[2], Kaoru Kawakami[1], Mahiro Sasage[2], Sakiko Ishino[3,11] ✉, Shohei Hattori[4,5,11] ✉, Ryu Uemura[6], Hitoshi Matsui[6], Koji Fujita[6], Naga Oshima[7], Andrea Spolaor[8], Anders Svensson[9], Bo Møllesøe Vinther[9], Hiroshi Ohno[10], Osamu Seki[1] & Sumito Matoba[1]

Anthropogenic NO_x emissions have altered the biogeochemical nitrogen cycle since the Industrial Revolution, yet Arctic ice core nitrate (NO_3^-) records are inconsistent with post-1970s NO_x emission reductions. Here we show a NO_3^- deposition history covering 1800–2020 using an ice core from the south-eastern Greenland dome with high snow accumulation. The ice core NO_3^- concentrations are particularly disconnected from NO_x source regions during the peak pollution period and post-1990s. A global chemical transport model reproduced these discordances between total NO_3^- and NO_x emissions by altering gaseous HNO_3 and particulate NO_3^- (p-NO_3^-) ratios and subsequently NO_3^- lifetime. This result and correlations with acidity parameters recorded in the ice core, suggest that acidity-driven gas-particle partitioning of NO_3^- regulates its transport to Arctic regions alongside changes in NO_x emissions. In the future, despite NO_x reductions, the increase in proportion of p-NO_3^- with longer atmospheric lifetime becomes crucial to control the Arctic NO_3^- burden.

NO_3^- and its precursors (NO_x = NO + NO_2) play important roles for both the atmosphere (i.e., particulate matter[1], climate system[2,3], and oxidative capacity through the formation of ozone (O_3)[4]) and biosphere[5,6]. Global atmospheric models all agree that anthropogenic activities have resulted in a dramatic increase in atmospheric NO_3^- burden through the Industrial Era[2,7,8], although the magnitude of the increase remains highly uncertain owing to order of magnitude variability in atmospheric NO_3^- burden among models[9,10]. Despite efforts to curb NO_x emissions in recent decades, the unexpectedly slow particulate NO_3^- reduction in a wide area of the Northern Hemisphere underscores the importance of understanding atmospheric NO_3^- dynamics beyond precursor NO_x emission[11–14].

Atmospheric NO_3^- exists as gaseous HNO_3 and particulate NO_3^- (p-NO_3^-). While both forms can undergo wet and dry depositions[15], HNO_3 is more readily removed due to its high solubility, whereas the p-NO_3^-, generally in the form of NH_4NO_3 in fine-mode particles, is less prone to local deposition and supports long-range transport[16]. Thus, the shift in gas–particle partitioning toward p-NO_3^-, driven by physical

[1]Institute of Low Temperature Science, Hokkaido University, Sapporo, Japan. [2]Graduate School of Environmental Science, Hokkaido University, Sapporo, Japan. [3]Institute of Nature and Environmental Technology, Kanazawa University, Kanazawa, Japan. [4]International Center for Isotope Effects Research (ICIER), Nanjing University, Nanjing, China. [5]State Key Laboratory of Critical Earth Material Cycling and Mineral Deposits, Frontiers Science Center for Critical Earth Material Cycling, School of Earth Sciences and Engineering, Nanjing University, Nanjing, China. [6]Graduate School of Environmental Studies, Nagoya University, Nagoya, Japan. [7]Meteorological Research Institute, Tsukuba, Japan. [8]Institute of Polar Sciences, National Research Council of Italy (ISP-CNR), Venezia-Mestre 30172, Italy. [9]Center for Ice and Climate, Section for the Physics of Ice, Climate, and Earth, Niels Bohr Institute, University of Copenhagen, Copenhagen, Denmark. [10]Kitami Institute of Technology, Kitami, Japan. [11]These authors contributed equally: Yoshinori Iizuka, Sakiko Ishino, Shohei Hattori. ✉e-mail: iizuka@lowtem.hokudai.ac.jp; ishino-sakiko@se.kanazawa-u.ac.jp; hattori@nju.edu.cn

factors, such as liquid water content and temperature and by chemical factors like atmospheric acidity—especially changes in aerosol pH—can influence the distribution and deposition pattern of NO_3^-[12,17–19]. In recent decades, the persistent accumulation of atmospheric p-NO_3^- due to atmospheric neutralisation has been observed in the vicinity of anthropogenic NO_x source regions[12,14,20]. These studies have primarily focused on the persistence of particulate matter from the perspective of air quality in major source regions, often highlighting the buffering effect of gas-particle partitioning in maintaining p-NO_3^- concentrations despite reductions in NO_x and SO_2 emissions. In contrast, over longer timescales—particularly since the Industrial Revolution, including periods of dramatic atmospheric acidification—the impact of this buffering mechanism on the long-range transport, spatial distribution, and deposition of NO_3^- in remote regions sensitive to environmental changes (e.g., the Arctic) remains poorly understood.

Greenland ice cores are archives for reconstructing changes in atmospheric species in response to anthropogenic activities in the Northern Hemisphere[21–23]. The atmospheric NO_3^- in the Arctic region is mainly removed through wet deposition[24–26] and deposits on the ice sheet. However, NO_3^- concentration (hereafter [NO_3^-]) in Greenland ice cores are influenced not only by atmospheric deposition[23] but also by post-depositional processes such as photolytic loss and subsequent recycling[27–29]. In addition, snow accumulation in central Greenland (e.g., Summit site) is dominated by summer snow[30], introducing seasonal bias to NO_3^- deposition associated with seasonally distinct NO_x sources. Due to these uncertainties, while the increase in Greenland ice core [NO_3^-] since the Industrial Revolution is attributed to anthropogenic activities[21], a decrease in ice core [NO_3^-] has not been clearly observed despite the suppression of NO_x emissions since the 1970s[31], and these factors have not yet been comprehensively interpreted at a mechanistic level.

The ice core from the Greenland SE-Dome region (67.18°N, 36.37°W, 3170 m a.s.l.), drilled to 90 m in 2015 (SE-Dome I[32]) and to 250 m in 2021 (SE-Dome II[33]), is contextually highly desirable owing to its high accumulation rate at ~1 m yr^{-1} in water equivalents[34,35], the highest among Antarctic and Greenland ice domes. The SE-Dome region is characterised by minimal post-depositional NO_3^- loss, as regions with snow accumulation rates exceeding 50 cm yr^{-1} in water equivalents typically bury deposited NO_3^- within approximately half a month[34,36]. Furthermore, regional snow accumulation is constant throughout the year[34] (Supplementary Fig. S1), suggesting a negligible seasonal bias for NO_3^- deposition. Here, we reconstructed seasonally resolved NO_3^- deposition history from the SE-Dome II ice core covering 220 years (1800 to 2020 AD) from pre-industrial times (PI) to present-day (PD). By comparing the well-preserved atmospheric SE-Dome II NO_3^- records with NO_x emission inventories from source regions, we determined that, in addition to precursor NO_x emission changes, variations in atmospheric acidity influence the magnitude of NO_3^- transport and deposition to Arctic regions by altering the gas-particle partitioning.

Results

Annual average [NO_3^-] from 1800 to 2020 in SE-Dome II ice core

Annual [NO_3^-] in the SE-Dome II ice core are presented in Fig. 1a. Pursuant to a previous study[37], the present study focused on concentrations, which more accurately reflect atmospheric abundance in high accumulation areas than the flux. The annual [NO_3^-] of the SE-Dome II was 24.4 ± 9.2 μg kg^{-1} on average for 1801–1850 (PI), increasing from the 1850s to reach a maximum of 72.0 ± 18.9 μg kg^{-1} from 1971 through 2000. After the 2000s, [NO_3^-] decreased slightly but maintained high values (65.7 ± 14.1 μg kg^{-1}) between 2011 and 2020. NO_3^- flux trends in the SE-Dome I ice core for 1960–2014[31] showed similar interannual variability (see Supplementary Notes (SN) 1, Supplementary Fig. S2), ensuring the robustness of our data. By defining the 1970–2000 period as the peak of anthropogenic NO_3^- deposition in Greenland [pollution peak (PP)][23], with 1800–1850 as the PI baseline, a [NO_3^-] ratio of 2.91 between these periods was obtained.

Comparison between ice core NO_3^- and NO_x emission inventory

To focus on the variation in anthropogenic NO_3^-, which is primarily influenced by human activities such as fossil fuel combustion, industrial emissions, and agriculture-related fertilisation, the [NO_3^-] trend was normalised after subtracting the 1800–1850 (PI) average, which represents the baseline level of natural NO_3^- (see Methods). Figure 1b shows the comparison between normalised [NO_3^-] and anthropogenic NO_x emission inventories from the Former Soviet Union (FSU), North America (NA), and Europe (EU) and provides a trendline with their combination (TRAJ). Despite the increase in Asian NO_x emissions after the 2000s, the Asian contribution to NO_3^- in the SE-Dome region remained minimal and did not affect the main conclusion of this study (see SN 2 and Supplementary Fig. S3).

Normalised [NO_3^-] peaked at approximately 3 at PP (1970–2000) (Fig. 1b). The normalised NO_x emission inventories for EU, NA, and TRAJ showed similar increases of 3–4 in PP but were relatively higher at up to 5 for FSU. The NO_x emissions from TRAJ regions roughly agree with the [NO_3^-] increase from PI to PP, indicating that the [NO_3^-] trend from 1800 to 2020 was primarily driven by anthropogenic NO_x emissions from surrounding countries, although the peak [NO_3^-] remains slightly lower than that of the surrounding regions. [NO_3^-] began increasing from 1870 to 1920 before the increase in NO_x emissions (Fig. 1b). This discrepancy and its cause have been discussed elsewhere[38](see SN 3).

The [NO_3^-] and NO_x emission trends thus show general agreement; however, the [NO_3^-] increase in the SE-Dome from 1920 to 1970 was more gradual than the corresponding rise in NO_x emissions (Fig. 1b). Conversely, the [NO_3^-] decrease after the 1990s was slower than the significant reductions in NO_x emissions (Fig. 1b). This slow response of [NO_3^-] to drastic changes in NO_x emission is a contrasting result to the case of [SO_4^{2-}] in ice cores that corresponds well with that of SO_2 emission in surrounding countries[39]. This result highlights that there are other factors controlling the magnitude of NO_3^- transported to the Arctic region from the precursor NO_x emissions.

The PP/PI ratios of [NO_3^-] in other Greenland ice cores were about 2 or lower (Supplementary Figs. S2, S4, see SN 4) possibly due to geographical reasons (e.g., distance from the source regions), post-depositional NO_3^- losses[23] and/or seasonal bias due to summertime snow accumulation[30]. Notably, the [NO_3^-] trends among several Greenland ice cores during the Industrial Era were similar to those of the SE-Dome ice core; [NO_3^-] increased more slowly from 1940 to 1970 and decreased more slowly after the 1990s than NO_x emissions (Supplementary Fig. S2). This similarity ensures the spatial robustness of the discordance between [NO_3^-] and NO_x over Greenland, not merely a local phenomenon at the SE-Dome site (see SN 4).

Correlation between $\Delta(NO_3^- - NO_x)$ and ice core chemistry

We investigated the 30 years running mean of the difference between normalised ice core [NO_3^-] and the annual normalised NO_x emissions [$\Delta(NO_3^- - NO_x)$] (Fig. 2a). The $\Delta(NO_3^- - NO_x)$ showed negative and positive values during 1920–1970 and 1990–2020, respectively. To identify the factors explaining the pattern and discordance between NO_x emission to [NO_3^-] records, $\Delta(NO_3^- - NO_x)$ was compared with the various chemical and meteorological factors that could affect the transport behaviour of atmospheric NO_3^- (Fig. 3 and Supplementary Fig. S5, and SN 5). In this correlation assessment, the period prior to 1920 was excluded due to the low [NH_4^+] data (often below the detection limit), the lack of meteorological data before 1900, and the aforementioned issue with the reliability of NO_x emission inventory between 1870 and 1920 (see SN 3).

https://doi.org/10.1038/s41467-025-59208-0

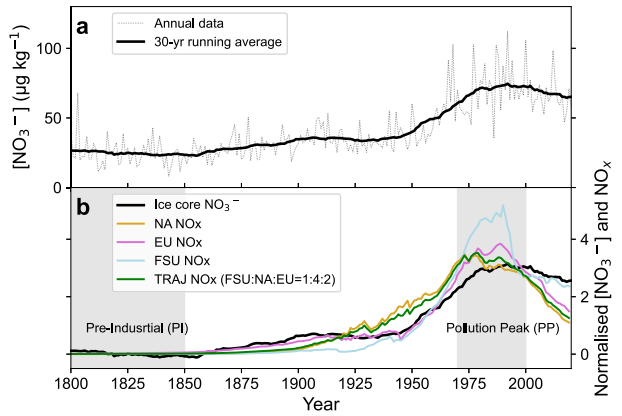

Fig. 1 | Annual $[NO_3^-]$ at the SE-Dome and NO_x emission inventory from 1800 to 2020. a Annual (grey dot) and 30-year running average (black) of $[NO_3^-]$. **b** Normalised 30-year running average of $[NO_3^-]$ (black), and anthropogenic NO_x emissions from North America (NA, orange), Europe (EU, purple), and the Former Soviet Union (FSU, light blue). Trajectory-based blend (TRAJ, green) from the Former Soviet Union: North America: Europe = 1:4:2 according to the air-mass origins calculated via quantitative back-trajectory analysis[31].

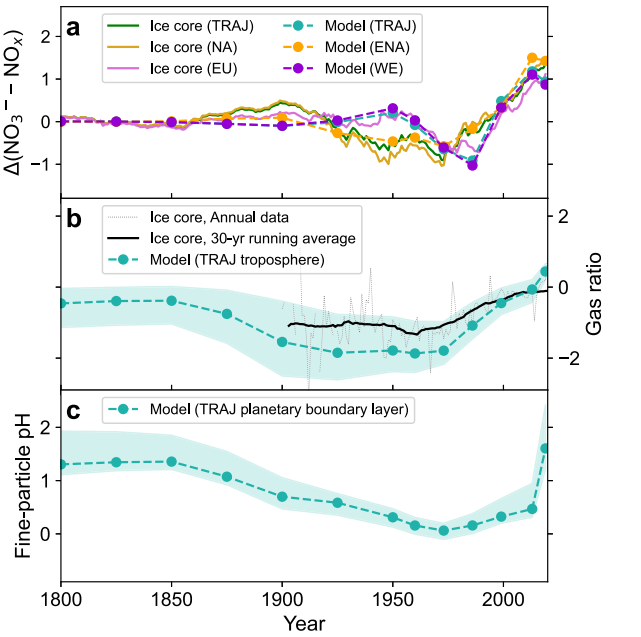

Fig. 2 | Ice core and model comparison of temporal changes in the difference between normalised $[NO_3^-]$ and NO_x emission ($\Delta(NO_3^- - NO_x)$) and acidity related parameters. a $\Delta(NO_3^- - NO_x)$ derived from ice core records (solid lines) and GEOS-Chem simulations (dashed lines). The solid lines were calculated using the ice core $[NO_3^-]$ compared with CEDS NO_x emissions from North America (NA, orange), Europe (EU, purple), and trajectory-based blend (TRAJ, green) regions. The dashed lines were calculated from the modelled NO_3^- deposition in the SE-Dome grid compared with CEDS NO_x emissions in the model for Eastern North America (ENA, orange), Western Europe (WE, purple), and TRAJ regions (TRAJ, blue-green). **b** Gas ratio (GR): $([NH_4^+]-2[nss\text{-}SO_4^{2-}])/[NO_3^-]$ for ice core observation (grey, annual data; black, 30 years running average), and $([NH_4^+]+[NH_3]-2[nss\text{-}SO_4^{2-}])/([p\text{-}NO_3^-]+[HNO_3])$ from the modelled annual mean tropospheric concentrations over TRAJ region (blue-green). **c** Modelled planetary boundary layer mean aerosol pH for fine-mode particles over the TRAJ region (blue-green). Markers and shadows in (**b**, **c**) represent median and inter-quartile range, respectively, of variables over the model grids in the TRAJ region (− 90° to 30°E and 45° to 90°N, $n = 300$).

Among the variables, the $\Delta(NO_3^- - NO_x)$ after 1920 was significantly ($p < 0.01$) correlated with the atmospheric acidity-related parameters and cation species preserved in the ice core: ionic balance $[H^+]$ ($r = -0.41$, Fig. 3a), $[nss\text{-}SO_4^{2-}]$ ($r = -0.52$, Fig. 3b), gas ratio (GR, defined as $([NH_4^+]-2[nss\text{-}SO_4^{2-}])/[NO_3^-]$[15]) ($r = 0.65$, Fig. 3c) and $[Ca^{2+}]$ ($r = 0.60$, Fig. 3d), while the lack of a significant correlation to meteorological factors, such as air temperature over the North Atlantic regions ($r = 0.17$) and NAO index ($r = 0.25$) (Supplementary Fig. S5). These results imply that the change of the $\Delta(NO_3^- - NO_x)$ were related to chemical processes after NO_x emissions, rather than changes in atmospheric dynamics nor meteorological conditions.

NO_3^- exists in two forms, HNO_3 and p-NO_3^-, which have different lifetimes and deposition velocities, and changes in their partitioning can significantly influence the amount of NO_3^- transported over long distances[12,17,18]. This gas-particle partitioning is primarily governed by the acidity and liquid water content of fine-mode aerosols[40,41]. In fact, as shown in Fig. 3a, b, $\Delta(NO_3^- - NO_x)$ showed a stronger correlation with $[nss\text{-}SO_4^{2-}]$, the main driver of fine-mode aerosol acidity[15], than that with $[H^+]$, which does not necessarily represent the acidity of fine-mode aerosols due to the influence of coarse-mode ions, such as Ca^{2+} and Na^+ originating from mineral dust and sea salt[42]. Furthermore, the observed higher correlation with GR (Fig. 3c), which is a simple representation of free ammonia available for NH_4NO_3 particle formation[15,43], further supports the above-mentioned process driven by changes in atmospheric acidity. Other acidity-related parameters, such as $[NH_4^+]/[nss\text{-}SO_4^{2-}]$, also showed significant correlations (Supplementary Fig. S5, see SN 5). The more accurate proxy of free ammonia, adjusted gas ratio (adjGR, defined as $([NH_3]+[NO_3^-])/([HNO_3]+[NO_3^-])$)[44], is not applicable because it requires separate p-NO_3^- and HNO_3 concentrations, which are not available from $[NO_3^-]$ in the ice core representing a mixture of both.

The correlation with $[Ca^{2+}]$ (Fig. 3d), primarily from mineral dust, suggested that the uptake of HNO_3 by coarse-mode dust particles also led to efficient dry deposition of NO_3^- onto the ice sheet. However, the correlation with $[Ca^{2+}]$ became significantly stronger only after the 1990s, when $[Ca^{2+}]$ and insoluble dust concentration in the SE-Dome I ice core began to rise as a result of emissions from local coastal Greenland[45]. Notably, limited amount of Ca^{2+} in the ice core available to pair with NO_3^- (Supplementary Fig. S6 and SN 6) indicates that this process was of secondary importance in explaining $\Delta(NO_3^- - NO_x)$.

Acidity-driven partitioning of HNO_3 and p-NO_3^- in the GEOS-Chem model

To examine the importance of gas-particle partitioning between HNO_3 and p-NO_3^- in changes in transport and deposition patterns of total NO_3^- in response to anthropogenic emissions, global tropospheric chemistry was simulated using the GEOS-Chem chemical transport model. In the historical experiment, the meteorological fields were fixed to those in 1986 and only emissions were varied from 1800 to 2019 (see Methods), and responses of spatial and temporal variations of atmospheric NO_3^- were investigated. Throughout the entire period, atmospheric total NO_3^- (sum of HNO_3 and p-NO_3^-) deposition at the SE-Dome site in the model was predominantly derived from wet deposition (Fig. 4w and Supplementary Fig. S7), consistent with observations in the Arctic[24–26]. Figure 2a shows the modelled $\Delta(NO_3^- - NO_x)$ values using sum of wet and dry NO_3^- depositions in the SE-Dome grid and NO_x emissions from different source regions (ENA, WE, and TRAJ). The modelled $\Delta(NO_3^- - NO_x)$ values were relatively constant until 1950, decreased until 1986, and increased up to PD, aligning with the observed post-1950 trend (Fig. 2a). This pattern covaried with the modelled GR values (Fig. 2b), and consequently aerosol pH in TRAJ region (Fig. 2c). We note that the temporal variations in aerosol pH are consistent with those reported by Zhai et al. [46], showing a more gradual increase in pH after the PP compared to the change from PI to PP. Thus, the modelled $\Delta(NO_3^- - NO_x)$ trends largely reproduced those observed in the SE-Dome ice core (Fig. 2a) and confirmed a connection with the

https://doi.org/10.1038/s41467-025-59208-0

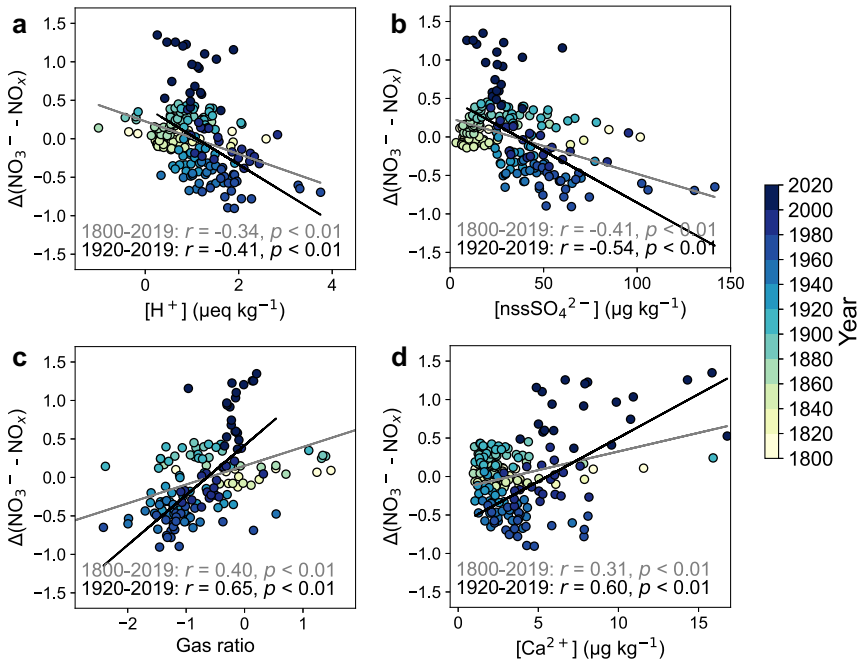

Fig. 3 | Scatter plots of the difference between normalised $[NO_3^-]$ and normalised NO_x emission in the TRAJ region $[\Delta(NO_3^- - NO_{x\ TRAJ})]$ as functions of atmospheric acidity related parameters in the SE-Dome II ice core. $\Delta(NO_3^- - NO_{x\ TRAJ})$ was compared to (**a**) ionic balance $[H^+]$ $\{([NO_3^-] + [Cl^-] + 2[SO_4^{2-}]) - ([NH_4^+] + [Na^+] + 2[Ca^{2+}])\}$ (μmol kg^{-1}), (**b**) $[nss\text{-}SO_4^{2-}]$ (μg kg^{-1}), (**c**) gas ratio (GR) (mol mol^{-1}), and (**d**) $[Ca^{2+}]$ (μg kg^{-1}). The colour scale represents the year. Regression lines were fitted for the periods 1800–2019 (grey) and 1920–2019 (black).

partitioning of HNO_3 and p-NO_3^- between acidity related parameters and $\Delta(NO_3^- - NO_x)$.

Based on this result, we investigated the changes in transport and deposition patterns of NO_3^- in the model (Fig. 4). The modelled surface p-NO_3^- to total-NO_3^- ratio (ε) in ENA, WE, and TRAJ regions commonly declined during PP (1973, Fig. 4j) and increased after NO_x reduction (2013, Fig. 4n). Reflecting a faster dry deposition rate of HNO_3 than that of p-NO_3^-[16], the changes in ε values resulted in the increased dry deposition ratio to total NO_3^- deposition from PI (1850 and 1900, Fig. 4 c and g) to PP (1973, Fig. 4k) and its decrease to PD (2013 and 2019, Fig. 4o and s) in these three regions (Fig. 4w). Because of the changes in deposition velocity, the lifetime (τ_{NO3}) of t-NO_3^- also decreased until 1973 (Fig. 4l), followed by an increase through PD (2019) (Fig. 4t), as shown in Fig. 4x. These results are consistent with the role of gas-particle partitioning in nitrate transport discussed by Geng et al.[19], in the regard that HNO_3 is more abundant than p-NO_3^- and its fraction increased during PP. However, our findings suggest that the rapid dry deposition of HNO_3 near source regions limits its long-range transport, altering the overall magnitude of NO_3^- transported over long distances. This contrasts with the mechanism proposed by Geng et al.[19], which assumes that low-$\delta^{15}N$ HNO_3 is preferentially transported and preserved in ice cores. Further research is needed to fully verify these differences. Overall, the model represents the evolution of atmospheric acidity leading to the changes in gas-particle partitioning of HNO_3 and p-NO_3^-, reasonably explaining changes in NO_3^- transport and the $\Delta(NO_3^- - NO_x)$.

Notably, the changes in ε and dry deposition ratio were less pronounced in WE than those in ENA (Fig. 4v and w). The intriguing differences between ENA and WE are likely due to variations in relative humidity and acidity, which regulate their dry deposition velocity as discussed by Nenes et al.[16] (see Supplementary Fig. S7 and SN 7). The tropospheric concentration of peroxyacetyl nitrate (PAN), a dominant species in atmospheric reactive nitrogen whose thermal decomposition is possibly a non-negligible NO_x source in the Arctic region[47], responded linearly to anthropogenic NO_x emissions (Supplementary Fig. S8) and did not serve as an explanatory factor to the variability of the modelled $\Delta(NO_3^- - NO_x)$ (see SN 8).

Potential factors controlling NO_3^- transport and limitations of the model

Nonetheless, there are still limitations in the model regarding the effects of acidity and the associated gas-particle partitioning. Indeed, certain discrepancies remain between observation and model results in this study (see Fig. 2a and Supplementary Fig. S9 and SN 9), with the most critical issue being the overestimation of the modelled NO_3^- deposition in SE-Dome region compared to the observed ice core $[NO_3^-]$ after 1920s by approximately a factor of 2 (Supplementary Fig. S9c). This could be associated with a long-standing problem of an overestimate of t-NO_3^- in the remote atmosphere in the model[18], with recent studies suggesting that this may be attributed to an underestimation of the rainout and washout processes for nitric acid and nitrate[48]. Incorporating these deposition processes into the future model is expected to reduce the discrepancy between the model and ice core NO_3^- concentrations.

However, other limitations exist in this study, which will need to be addressed in future research. The gas-particle partitioning in GEOS-Chem used in this study was governed by the aerosol thermodynamic model ISORROPIA II, which mainly accounted for the formation of fine-mode NH_4NO_3[49,50]. With these models, a large uncertainty remained in the pH calculations, particularly regarding cation components, such as Na^+ and Ca^{2+} as pointed out by Pye et al. [15]. Notably, $[Ca^{2+}]$ and $[Na^+]$ had increased in the SE-Dome ice core since 1990 (Supplementary Fig. S6), but these components were not accurately considered in the model. Furthermore, the model did not capture possible changes in the formation of coarse-mode p-NO_3^- on mineral dust or sea salt, such as in the form of $Ca(NO_3)_2$ and $NaNO_3$, which proceeded efficient dry deposition compared to fine-mode particles[51]. They could both decrease and increase the modelled ice core $[NO_3^-]$ concentrations.

https://doi.org/10.1038/s41467-025-59208-0

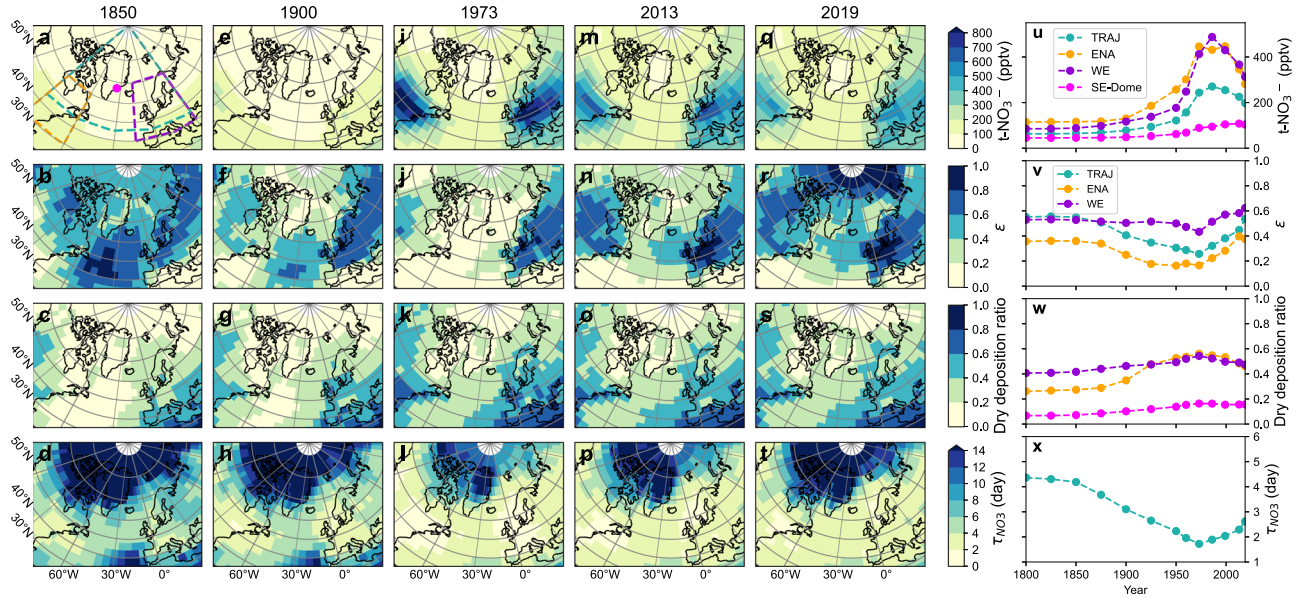

Fig. 4 | Modelled historical changes in NO_3^- transport and deposition patterns. **a**–**t** Spatial distributions in annual mass-weighted average of tropospheric total NO_3^- (t-NO_3^-) (**a**, **e**, **i**, **m**, **q**), particulate NO_3^- (p-NO_3^-) ratio to t-NO_3^- (ε) in the surface layer (**b**, **f**, **j**, **n**, **r**), dry deposition ratio to t-NO_3^- deposition (**c**, **g**, **k**, **o**, **s**), and atmospheric lifetime of t-NO_3^- (τ_{NO3}, defined as the column amount divided by the deposition flux) (**d**, **h**, **l**, **p**, **t**) in 1850 (**a**–**d**), 1900 (**e**–**h**), 1973 (**i**-**l**), 2013 (**m**–**p**), and 2019 (**q**–**t**). **u**–**x** Regional averages of tropospheric t-NO_3^- concentration (**u**), surface ε (**v**), dry deposition ratio (**w**), and τ_{NO3} (**x**). Different line colours in (**u**–**x**) represent variables averaged over different regions: 10-day back trajectory region from SE-Dome (TRAJ, bluegreen), Eastern North America (ENA, orange), Western Europe (WE, purple), and SE-Dome grid (magenta), as indicated in (**a**).

The decrease could occur by shortening the overall lifetime through an increase in the coarse-mode p-NO_3^- fraction during transport, while the increase could be due to promoting dry deposition over the Greenland ice sheet. We note that the model sensitivity test considering HNO_3 uptake on dust particles[18] resulted in less than a 2% decrease in t-NO_3^- depositions in the SE-Dome grid. However, this is a conservative estimate, due to the uncertainties in the uptake coefficient and the absence of high-latitude dust sources in the model[52] (see SN 9).

Other parameters must also be taken into account for factors beyond changes in atmospheric acidity. The model used in this study was unlikely to accurately capture decadal changes in aerosol liquid water content, which is another key factor influencing the gas-particle partitioning of NO_3^-[41], due to the fixed meteorological field including temperature and humidity (see Methods and SN 9). Although PAN was not necessarily critical in reproducing the variation of the $\Delta(NO_3^- - NO_x)$ values in this model, considering the impacts of the recent global warming, especially in the Arctic, temperature-dependent PAN decomposition could influence the spatiotemporal variability of PAN-derived NO_x and NO_3^- deposition (see SN 8). In addition, the GEOS-Chem model version used in the present study did not account for recent findings, such as increased reactive nitrogen lifetime due to NO_3^- photolysis[53–55], although this process itself does not completely explain the discrepancy (SN 9).

Overall, while this study broadly reproduced the $\Delta(NO_3^- - NO_x)$ values and highlighted the importance of atmospheric acidity in modifying gas-particle partitioning, factors including those mentioned above should be carefully considered in future models to accurately capture the magnitude of long-range transport of reactive nitrogen to remote regions like the Arctic. The reconstructed NO_3^- deposition in SE-Dome II provides a valuable archive to constrain these uncertainties.

This study reconstructed the variations from the pre-industrial era to the present using NO_3^- records from SE-Dome ice core, which is characterised by minimal post-depositional NO_3^- loss and seasonal biases. It demonstrated that these NO_3^- variations reflect not only changes in NO_x emissions in the source regions but also shifts in gas-particle partitioning driven by changes in atmospheric acidity. In particular, we revealed that changes in atmospheric acidity alter the atmospheric lifetime of total nitrate (t-NO_3^-), thereby controlling its long-range transport and subsequent deposition patterns in remote regions. While the dampening of atmospheric p-NO_3^- reduction caused by increased NH_3 and decreased SO_2 emissions is now recognised in major anthropogenic regions in the world[11–14,17,20], our results suggest that the scale of this impact may be hemispheric as evidenced in long-term aerosol p-NO_3^- observations at Alert[56]. This trend in anthropogenic emission change is predicted to continue through 2050 under the Shared Socioeconomic Pathways (SSP) 2-4.5 scenario[57]. Furthermore, the SE-Dome ice-core record indicates that NO_3^- has become the dominant inorganic anion in the Arctic aerosols since the 1990s, mirroring decreased SO_2 emissions and SO_4^{2-} concentrations (Supplementary Fig. S6). Considering that the net climate impacts of reactive nitrogen due to aerosol scattering of solar radiation and oxidants supply for regulating greenhouse gas lifetimes[3], the persistent t-NO_3^- loading in the Arctic atmosphere is a critical issue in this climatically sensitive region[58]. In addition, air quality and climate concerns involve impacts on O_3 burden due to the significant role of p-NO_3^- photolysis in O_3 formation in remote and Arctic regions[53–55].

With regard to accurate future predictions and assessments of atmospheric NO_3^-, minimising uncertainties associated with transport and deposition patterns of NO_3^- in chemical transport models is crucial. However, the inter-model variability of NO_3^- simulation remains larger than that for SO_4^{2-}, largely owing to the different representations of gas-particle partitioning for both fine-mode and coarse-mode p-NO_3^- among models[10]. Although our comparison of ice core observations and GEOS-Chem modelling suggests good overall agreement, feedback from acidity-driven changes in NO_3^- lifetime by modifying gas-particle partitioning may be overestimated in the model. Multi-phase chemistry dependent on atmospheric acidity remains a significant challenge in atmospheric chemistry, with high uncertainty for atmospheric dry NO_3^- deposition[15].

Reducing this uncertainty requires refining atmospheric acidity modelling, gas-particle partitioning, and HNO_3 and p-NO_3^- atmospheric lifetimes. An increased dust supply from the Greenland margin areas after 2000[45,52] could add significant uncertainty to the deposition pattern of NO_3^- through the HNO_3 acid uptake. The [NO_3^-] record from the SE-Dome II ice core, reported herein, provides a uniquely well-preserved and high temporal resolution archive essential for validating such key model parameters.

Methods

SE-Dome II ice core and age scale

We used a 250 m depth ice core obtained at a dome site on the SE-Dome (67.18°N, 36.37°W, 3170 m a.s.l[33].). The annual mean temperature at the SE-Dome was − 20.9 °C[32]. For a timescale, we used the age scale for 1800–2020 determined by Kawakami et al.[35]. The age scale was carefully evaluated using independent age markers and its precision was within a half year and could thus produce precise ion concentrations and/or flux in annual resolution.

Analytical method of ion concentrations

In a cold room (class 10000) at the Institute of Low Temperature Science, Hokkaido University, Japan, the ice core was divided into 50 mm-depth sections, except for the top 5 m, where the low firn density necessitated 100 mm sections, using a clean ceramic knife, put into a cleaned polyethene bottle, and melted at + 20 °C in a clean room. Ion concentrations (Cl^-, SO_4^{2-}, NO_3^-, Na^+, Ca^{2+}, and NH_4^+) were measured using ion chromatography [Thermo Scientific ICS-2100 (Thermo Fisher Scientific, Waltham, MA, USA); Dionex CS-12A column (Thermo Fisher Scientific) and 20 mM MSA eluent for cations; Dionex AS-18A column (Thermo Fisher Scientific) and 23-mM KOH eluent for anions]. The injection volume was 1000 μL for anions and 500 μL for cations. The analytical precision for ion concentration measurements was 10%, and the detection limit was 0.1 μg kg^{-1} for NO_3^-. A total of 4948 samples, covering AD 1800 to 2020, were analysed, corresponding to 23 samples per year on average. In several samples, the Cl^-, SO_4^{2-}, NO_3^-, Na^+, Ca^{2+}, and NH_4^+ concentrations were below the detection limit and were thus regarded as zero. To confirm that analytical errors did not cause any large peak in ion concentrations, samples with significantly different values from two adjacent samples, based on a 3-point running standard deviation (> 3σ), were re-measured with another ice sample from the same depth. Surface decontamination and sample melting were conducted within 1 week and 1 day, respectively, of the ion chromatography measurement.

Calculation of annual [NO_3^-] and the related ion concentrations, normalised [NO_3^-] and NO_x emissions

The [NO_3^-] (n = 4948) were averaged per year (n = 221; from 1800 to 2020), as a boundary on 1 January from the age scale[35]. The annual [NO_3^-] average error was roughly 2% (10 /$\sqrt{22}$), depending on the analytical error (10%) and number of data averaged (n = 22). Annual [Cl^-], [SO_4^{2-}], [Na^+], [NH_4^+], and [Ca^{2+}] were calculated in the same manner. Ionic balance (H^+ concentration) was calculated as the difference of total anion minus total cation concentrations {[Cl^-] + 2[SO_4^{2-}] + [NO_3^-] − ([Na^+] + [NH_4^+] + 2[Ca^{2+}]) in μmol kg^{-1}}. Non-sea salt [SO_4^{2-}] ([nss-SO_4^{2-}], μmol kg^{-1}) were calculated by subtracting the sea-salt fraction ([ss-SO_4^{2-}] = 0.060 [Na^+]) from total [SO_4^{2-}], i.e., [nss-SO_4^{2-}] = [SO_4^{2-}] − [ss-SO_4^{2-}]. GR was calculated by [NH_4^+]−2[nss-SO_4^{2-}])/[NO_3^-] in molar ratio with assuming ice core [NO_3^-] and [NH_4^+] represent the sum of depositions of their gas and particulate form. Annual NO_3^- ion fluxes (n = 221; from 1800 to 2020) were based on the annual average [NO_3^-] value multiplied by the annual accumulation rate determined by Kawakami et al.[35]. The annual accumulation rate error depends on the density and timescale error used. This study used the timescale defined by Kawakami et al.[35], resulting in an error in density less than 1% per 1 mm, which is negligible compared with the [NO_3^-] error (2%).

In this study, to analyse the relative changes in anthropogenic NO_3^-, we distinguished between anthropogenic and natural sources of NO_3^- and normalised the data to allow for a comparable analysis of their changes. Anthropogenic NO_3^- primarily originates from NO_x emissions associated with industrial activities, such as the combustion of coal, oil, and natural gas. In addition, NO_3^- derived from soil NO_x emissions due to agricultural fertilisation was also considered an anthropogenic source. Natural NO_3^- sources includes lightning, biomass burning, and natural soil NO_x emissions. Whereas there is no observational evidence on the historical changes in natural NO_3^- sources, a modelling exercise considering all these anthropogenic and natural sources shows that more than 90% of global NO_x emission increases from PI to PD are driven by anthropogenic sources[59]. Furthermore, a global database of biomass burning emissions shows that the significant increase of biomass burning since 1990s are mainly at the tropics of South America and Asia, and that in North America and Europe regions are largely unchanged[60]. Therefore, we assumed that natural source NO_3^- remain constant throughout the entire period in the following process.

In the normalisation process, we first used the average ice core [NO_3^-] during the pre-industrial period (1800–1850) as the baseline for natural source NO_3^-. For each year, the baseline was subtracted from the annual mean ice core [NO_3^-] to estimate the anthropogenic NO_3^- contribution. We then normalised the annual anthropogenic NO_3^- values by dividing them with the average anthropogenic NO_3^- values over the entire period (1800–2020).

The anthropogenic NO_x emissions from multiple sectors, including agriculture, were obtained from the Community Emissions Data System (CEDS) inventory (http://globalchange.umd.edu/ceds/)[61,62]. The annual NO_x emissions of NA (orange in Fig. 1), EU (purple in Fig. 1), and FSU (blue in Fig. 1) were extracted. These data were also normalised by dividing by the average values for the period 1800–2020, making the NO_3^- and NO_x emission datasets comparable, since natural NO_x emissions are not included in the CEDS data. The TRAJ line (green in Fig. 1) was calculated as a blend of NA:EU:FSU = 4:2:1 following the air-mass contribution from NA, EU, FSU of 0.2, 0.1, 0.05, respectively, when the whole was set as 1, based on the 7-d back trajectory analysis using the HYSPLIT model[31].

Reanalysis climate data and index

The air temperature data were extracted from the Hudcurt5 reanalysis distributed by the Met Office Hadley Centre and the Climatic Research Unit at the University of East Anglia[63], and the relative humidity data from over-centennial atmospheric data assimilation (OCADA) reanalysis developed by the Meteorological Research Institute, Japan[64]. The annual air temperature anomalies (1895–2019) and tropospheric average of relative humidity (1900–2015) were extracted at the SE-Dome site (67.4°N, 36.4°W) and North Atlantic Ocean region (50–60°N, 25–55°W). We used the annual NAO index (1836-2019) distributed by the NOAA-CIRES-DOE Twentieth Century Reanalysis (20CR) project[65] and the annual AO index (1950–2015) distributed by NOAA, Climate Prediction Centre[66] for a proxy of climatic spatial pattern in the North Atlantic Ocean and Arctic Ocean, respectively.

GEOS-Chem chemical transport model

GEOS-Chem is a global three-dimensional atmospheric chemistry transport model (www.geos-chem.org) developed by Bey et al.[67]. GEOS-Chem version 12.5.0 (https://doi.org/10.5281/zenodo.3403111) driven by assimilated meteorological fields was used from the MERRA-2 reanalysis data product from NASA Global Modelling and Assimilation Office's GEOS-5 Data Assimilation System. To unravel variations driven by changes in anthropogenic emissions, a series of simulations

dating from 1800 to 2019 (1800, 1825, 1850, 1975, 1900, 1925, 1950, 1960, 1973, 1986, 1999, 2013, and 2019) at a 25-year temporal resolution before 1950 and 13-year temporal resolution after 1960 were conducted. According to the method of Hattori et al.[68], the models consider the same meteorology (year 1986) but changing anthropogenic and biomass burning emissions. For anthropogenic emissions, including soil emissions from agricultural sectors, the CEDS inventory was used[61,62], same as the NO_x inventory used for the comparison to ice core NO_3^-. Emission species from CEDS included aerosols [black carbon (BC) and organic carbon (OC)], aerosol precursors, and reactive compounds [SO_2, NO_x, NH_3, CO, and non-methane volatile organic carbon (NMVOC)]. The biomass-burning emissions were used from the CMIP6 inventory (BB4CMIP) for individual years[60]. Emission species from BB4CMIP included BC, CH_4, CO, NH_3, NMVOC, NO_x, OC, SO_2, and HCl. Note that the year-to-year variability of NO_x emission from BB4CMIP has the relatively small impact (~1%) to NO_3^- deposition at SE-Dome (see SN 9), ensuring our conclusion based on the modelling results is not influenced by the choice of year. Latitudinal CH_4 concentrations were prescribed for historical simulations. For years after 1979, CH_4 concentrations were based on the National Oceanic and Atmospheric Administration Earth System Research Laboratory (NOAA/ESRL) Global Monitoring Division flask observations http://esrl.noaa.gov/gmd/ccgg/trends_ch4/), and for years before 1979, the CMIP6 monthly mean surface CH_4 was used[69]. Dry and wet depositions of gas and aerosol species were simulated based on the general schemes in GEOS-Chem[70–72]. Peroxyacetyl nitrate (PAN), whose long-range transport and subsequent thermal decomposition supplies NO_x in the Arctic region[47], was simulated following Fischer et al.[73]. The model was spun up for 1 year before each of the years simulated.

The thermodynamic partitioning of HNO_3 to fine mode p-NO_3^- was computed using ISORROPIA II[49,50]. The module with assuming aerosol particles in the form of supersaturated solutions (i.e., the metastable state) and solving the forward problem using the total gas and aerosol concentrations of species as inputs (i.e., forward mode) to avoid the unrealistic aerosol pH[74]. The gas-particle equilibrium partitioning was computed every 20 min timestep in each grid. Because the meteorological fields are fixed and only emissions are varied in the historical experiments, the physical parameters used to calculate partitioning, such as temperature and relative humidity, are the same across years. The coarse mode p-NO_3^- is formed by the adsorption of HNO_3 on sea salt aerosols and is treated as a separate tracer than the fine mode p-NO_3^-[75]. The adsorption of HNO_3 on dust was not included in this study because of its limited impact within the dust outflow regions of the mid-latitude[18] and a lack of high-latitude dust sources in the model[18,52] (see SN 9).

The primary sources of NO_3^- to the Arctic region are Eastern North America (ENA) and Western Europe (WE). NO_x emissions were extracted over ENA (−90° to −60°E, 30° to 60°N, $n = 56$), WE (−15° to 40°E, 40° to 70°N, $n = 72$), and TRAJ (−90° to 30°E and 45° to 90°N, $n = 300$) (Fig. 4a) based on computed 10-d back trajectories according to a previous study[68]. NO_3^- deposition, including both dry and wet depositions, was extracted from the SE-Dome grid (−37.5° to −32.5°E, 62° to 66°N, $n = 1$) and converted to ice core [NO_3^-] by dividing by annual total precipitation. The modelled normalised [NO_3^-] in the SE-Dome grid and NO_x emissions from source regions were calculated in the same manner as those for ice core observations (see section above). To do this for the modelled [NO_3^-] and NO_x emissions, 220 annual values throughout the 1800–2019 period were calculated by interpolating the model results of the 13 discrete years.

GR from the model was calculated as $([NH_4^+] + [NH_3] - 2[SO_4^{2-}])/([p\text{-}NO_3^-] + [HNO_3])$, with considering gas and aerosol species separately unlike the ice core data, using the annual mean tropospheric concentrations over TRAJ region. Fine particle pH (recorded as Chem_phSav in the model) was also extracted for the TRAJ region and averaged over the boundary layer. The ratio of p-NO_3^- to t-NO_3^- (ε) was calculated as $\varepsilon = [p\text{-}NO_3^-] / ([p\text{-}NO_3^-] + [HNO_3])$ for the surface layer in the model. The atmospheric lifetime of t-NO_3^- (τ_{NO3}) was calculated in each horizontal grid by dividing the tropospheric column t-NO_3^- amount by the t-NO_3^- deposition flux.

Data availability

The ice core and model data generated in this study have been deposited in Figshare[76] (https://doi.org/10.6084/m9.figshare.25941562) and the Hokkaido University Collection of Scholarly and Academic papers, HUSCAP (http://hdl.handle.net/2115/94521). Source data are provided with this paper. Physical and chemical data, including ion concentration and flux of the SE-Dome I ice core, are available from HUSCAP (https://eprints.lib.hokudai.ac.jp/dspace/handle/2115/67127). The other ice core data supporting the findings of this study are publicly available online as follows: Summit, NEEM, and EGRIP data were cited from https://doi.org/10.1073/pnas.1319441111, https://doi.org/10.1594/PANGAEA.940553, and https://doi.org/10.1594/PANGAEA.945291, respectively. CEDS21 emissions data was from https://doi.org/10.5281/zenodo.4509372.

Code availability

The GEOS-Chem model version used in this study is available at https://doi.org/10.5281/zenodo.5500717. The Python codes and associated raw model outputs used for analyses are available upon request to the corresponding authors.

References

1. Cohen, A. J. et al. Estimates and 25-year trends of the global burden of disease attributable to ambient air pollution: an analysis of data from the Global Burden of Diseases Study 2015. *Lancet* **389**, 1907–1918 (2017).
2. Szopa, S. et al. in *Climate Change 2021 – The Physical Science Basis: Working Group I Contribution to the Sixth Assessment Report of the Intergovernmental Panel on Climate Change*. (Cambridge University Press, Cambridge, 2021).
3. Gong, C. et al. Global net climate effects of anthropogenic reactive nitrogen. *Nature* **632**, 557–563 (2024).
4. Finlayson-Pitts, B. J. & Pitts, J. N. in *Chemistry of the Upper and Lower Atmosphere*. (Academic Press, San Diego, 2000).
5. Galloway, J. N. et al. Transformation of the Nitrogen cycle: Recent trends, questions, and potential solutions. *Science* **320**, 889–892 (2008).
6. Duce, R. A. et al. Impacts of atmospheric anthropogenic Nitrogen on the open Ocean. *Science* **320**, 893–897 (2008).
7. Xu, L. & Penner, J. E. Global simulations of nitrate and ammonium aerosols and their radiative effects. *Atmos. Chem. Phys.* **12**, 9479–9504 (2012).
8. Hauglustaine, D. A., Balkanski, Y. & Schulz, M. A global model simulation of present and future nitrate aerosols and their direct radiative forcing of climate. *Atmos. Chem. Phys.* **14**, 11031–11063 (2014).
9. Gliß, J. et al. AeroCom phase III multi-model evaluation of the aerosol life cycle and optical properties using ground- and space-based remote sensing as well as surface in situ observations. *Atmos. Chem. Phys.* **21**, 87–128 (2021).
10. Bian, H. et al. Investigation of global particulate nitrate from the AeroCom phase III experiment. *Atmos. Chem. Phys.* **17**, 12911–12940 (2017).
11. Fagerli, H. & Aas, W. Trends of nitrogen in air and precipitation: Model results and observations at EMEP sites in Europe, 1980–2003. *Environ. Pollut.* **154**, 448–461 (2008).
12. Shah, V. et al. Chemical feedbacks weaken the wintertime response of particulate sulfate and nitrate to emissions reductions over the

eastern United States. *Proc. Natl. Acad. Sci. USA* **115**, 8110–8115 (2018).
13. Zhai, S. et al. Control of particulate nitrate air pollution in China. *Nat. Geosci.* **14**, 389–395 (2021).
14. Kim, H., Walters, W. W., Kysela, L. & Hastings, M. G. Long-term trends in inorganic aerosol chemical composition and chemistry at an urban and rural site in the northeastern US. *Sci. Total Environ.* **904**, 166848 (2023).
15. Pye, H. O. T. et al. The acidity of atmospheric particles and clouds. *Atmos. Chem. Phys.* **20**, 4809–4888 (2020).
16. Nenes, A. et al. Aerosol acidity and liquid water content regulate the dry deposition of inorganic reactive nitrogen. *Atmos. Chem. Phys.* **21**, 6023–6033 (2021).
17. Wu, C. et al. Different physicochemical behaviors of nitrate and ammonium during transport: a case study on Mt. Hua, China. *Atmos. Chem. Phys.* **22**, 15621–15635 (2022).
18. Fairlie, T. D. et al. Impact of mineral dust on nitrate, sulfate, and ozone in transpacific Asian pollution plumes. *Atmos. Chem. Phys.* **10**, 3999–4012 (2010).
19. Geng, L. et al. Nitrogen isotopes in ice core nitrate linked to anthropogenic atmospheric acidity change. *Proc. Natl. Acad. Sci. USA* **111**, 5808–5812 (2014).
20. Li, M. et al. Nonlinear responses of particulate nitrate to NO_x emission controls in the megalopolises of China. *Atmos. Chem. Phys.* **21**, 15135–15152 (2021).
21. Mayewski, P. A. et al. Sulfate and Nitrate concentrations from a South Greenland Ice Core. *Science* **232**, 975–977 (1986).
22. Legrand, M. & Mayewski, P. Glaciochemistry of polar ice cores: A review. *Rev. Geophys.* **35**, 219–243 (1997).
23. Röthlisberger, R. et al. Nitrate in Greenland and Antarctic ice cores: a detailed description of post-depositional processes. *Ann. Glaciol.* **35**, 209–216 (2002).
24. Bergin, M. H. et al. The contributions of snow, fog, and dry deposition to the summer flux of anions and cations at Summit, Greenland. *J. Geophys. Res. Atmos.* **100**, 16275–16288 (1995).
25. Fischer, H. & Wagenbach, D. Large-scale spatial trends in recent firn chemistry along an east-west transect through central Greenland. *Atmos. Environ.* **30**, 3227–3238 (1996).
26. Björkman, M. P. et al. Nitrate dry deposition in Svalbard. *Tellus B Chem. Phys. Meteorol.* **65**, https://doi.org/10.3402/tellusb.v65i0.19071 (2013).
27. Dibb, J. E., Whitlow, S. I. & Arsenault, M. Seasonal variations in the soluble ion content of snow at Summit. Greenland: Constraints from three years of daily surface snow samples. *Atmos. Environ.* **41**, 5007–5019 (2007).
28. Akers, P. D. et al. Sunlight-driven nitrate loss records Antarctic surface mass balance. *Nat. Commun.* **13**, 4274 (2022).
29. Jiang, Z., Alexander, B., Savarino, J., Erbland, J. & Geng, L. Impacts of the photo-driven post-depositional processing on snow nitrate and its isotopes at Summit, Greenland: a model-based study. *Cryosphere* **15**, 4207–4220 (2021).
30. Castellani, B. B., Shupe, M. D., Hudak, D. R. & Sheppard, B. E. The annual cycle of snowfall at Summit, Greenland. *J. Geophys. Res. Atmos.* **120**, 6654–6668 (2015).
31. Iizuka, Y. et al. A 60 year record of atmospheric aerosol depositions preserved in a high-accumulation Dome Ice Core, Southeast Greenland. *J. Geophys. Res. Atmos.* **123**, 574–589 (2018).
32. Iizuka, Y. et al. Glaciological and meteorological observations at the SE-Dome site, southeastern Greenland Ice Sheet. *Bull. Glaciol. Res.* **34**, 1–10 (2016).
33. Iizuka, Y. et al. Ice Core Drilling and the related observations at SE-Dome site, southeastern Greenland Ice Sheet. *Bull. Glaciol. Res.* **39**, 1–12 (2021).
34. Furukawa, R. et al. Seasonal-scale dating of a Shallow Ice Core From Greenland Using Oxygen Isotope matching between data and simulation. *J. Geophys. Res. Atmos.* **122**, 10,873–10,887 (2017).
35. Kawakami, K. et al. SE-Dome II Ice Core Dating with half-year precision: Increasing melting events from 1799 to 2020 in Southeastern Greenland. *J. Geophys. Res. Atmos.* **128**, e2023JD038874 (2023).
36. Zatko, M., Geng, L., Alexander, B., Sofen, E. & Klein, K. The impact of snow nitrate photolysis on boundary layer chemistry and the recycling and redistribution of reactive nitrogen across Antarctica and Greenland in a global chemical transport model. *Atmos. Chem. Phys.* **16**, 2819–2842 (2016).
37. Wolff, E. W. Chemical signals of past climate and environment from polar ice cores and firn air. *Chem. Soc. Rev.* **41**, 6247–6258 (2012).
38. Eckhardt, S. et al. Revised historical Northern Hemisphere black carbon emissions based on inverse modeling of ice core records. *Nat. Commun.* **14**, 271 (2023).
39. Moseid, K. O. et al. Using Ice Cores to evaluate CMIP6 aerosol concentrations over the historical Era. *J. Geophys. Res. Atmos.* **127**, e2021JD036105 (2022).
40. Guo, H. et al. Effectiveness of ammonia reduction on control of fine particle nitrate. *Atmos. Chem. Phys.* **18**, 12241–12256 (2018).
41. Nenes, A., Pandis, S. N., Weber, R. J. & Russell, A. Aerosol pH and liquid water content determine when particulate matter is sensitive to ammonia and nitrate availability. *Atmos. Chem. Phys.* **20**, 3249–3258 (2020).
42. Hennigan, C. J., Izumi, J., Sullivan, A. P., Weber, R. J. & Nenes, A. A critical evaluation of proxy methods used to estimate the acidity of atmospheric particles. *Atmos. Chem. Phys.* **15**, 2775–2790 (2015).
43. Ansari, A. S. & Pandis, S. N. Response of inorganic PM to precursor concentrations. *Environ. Sci. Technol.* **32**, 2706–2714 (1998).
44. Pinder, R. W., Dennis, R. L. & Bhave, P. V. Observable indicators of the sensitivity of PM2.5 nitrate to emission reductions—Part I: Derivation of the adjusted gas ratio and applicability at regulatory-relevant time scales. *Atmos. Environ.* **42**, 1275–1286 (2008).
45. Amino, T. et al. Increasing dust emission from ice free terrain in southeastern Greenland since 2000. *Polar Sci.* **27**, 100599 (2021).
46. Zhai, S. et al. Anthropogenic impacts on tropospheric reactive chlorine since the preindustrial. *Geophys. Res. Lett.* **48**, e2021GL093808 (2021).
47. Beine, H. J. & Krognes, T. The seasonal cycle of peroxyacetyl nitrate (PAN) in the European Arctic. *Atmos. Environ.* **34**, 933–940 (2000).
48. Luo, G., Yu, F. & Moch, J. M. Further improvement of wet process treatments in GEOS-Chem v12.6.0: impact on global distributions of aerosols and aerosol precursors. *Geosci. Model Dev.* **13**, 2879–2903 (2020).
49. Fountoukis, C. & Nenes, A. ISORROPIA II: a computationally efficient thermodynamic equilibrium model for K^+–Ca^{2+}–Mg^{2+}–NH_4^+–Na^+–SO_4^{2-}–NO_3^-–Cl^-–H_2O aerosols. *Atmos. Chem. Phys.* **7**, 4639–4659 (2007).
50. Pye, H. O. T. et al. Effect of changes in climate and emissions on future sulfate-nitrate-ammonium aerosol levels in the United States. *J. Geophys. Res. Atmos.* **114**, (2009).
51. Slinn, W. G. N. Some approximations for the wet and dry removal of particles and gases from the atmosphere. *Water Air. Soil Pollut.* **7**, 513–543 (1977).
52. Meinander, O. et al. Newly identified climatically and environmentally significant high-latitude dust sources. *Atmos. Chem. Phys.* **22**, 11889–11930 (2022).
53. Kasibhatla, P. et al. Global impact of nitrate photolysis in sea-salt aerosol on NO_x, OH, and O_3 in the marine boundary layer. *Atmos. Chem. Phys.* **18**, 11185–11203 (2018).
54. Shah, V. et al. Nitrogen oxides in the free troposphere: implications for tropospheric oxidants and the interpretation of satellite NO_2 measurements. *Atmos. Chem. Phys.* **23**, 1227–1257 (2023).

55. Shah, V. et al. Particulate Nitrate photolysis as a possible driver of rising tropospheric Ozone. *Geophys. Res. Lett.* **51**, e2023GL107980 (2024).
56. Sharma, S. et al. A factor and trends analysis of multidecadal lower tropospheric observations of arctic aerosol composition, Black Carbon, Ozone, and Mercury at Alert, Canada. *J. Geophys. Res. Atmos.* **124**, 14133–14161 (2019).
57. Gidden, M. J. et al. Global emissions pathways under different socioeconomic scenarios for use in CMIP6: a dataset of harmonized emissions trajectories through the end of the century. *Geosci. Model Dev.* **12**, 1443–1475 (2019).
58. Rantanen, M. et al. The Arctic has warmed nearly four times faster than the globe since 1979. *Commun. Earth Environ.* **3**, 1–10 (2022).
59. Murray, L. T. et al. Factors controlling variability in the oxidative capacity of the troposphere since the Last Glacial Maximum. *Atmos. Chem. Phys.* **14**, 3589–3622 (2014).
60. van Marle, M. J. E. et al. Historic global biomass burning emissions for CMIP6 (BB4CMIP) based on merging satellite observations with proxies and fire models (1750–2015). *Geosci. Model Dev.* **10**, 3329–3357 (2017).
61. Hoesly, R. M. et al. Historical (1750–2014) anthropogenic emissions of reactive gases and aerosols from the Community Emissions Data System (CEDS). *Geosci. Model Dev.* **11**, 369–408 (2018).
62. O'Rourke, P. R. et al. CEDS v_2021_02_05 Release emission data. Zenodo https://doi.org/10.5281/zenodo.4509372 (2021).
63. Morice, C. P. et al. An updated assessment of near-surface temperature change from 1850: The HadCRUT5 data set. *J. Geophys. Res. Atmos.* **126**, e2019JD032361 (2021).
64. Ishii, M. et al. Global historical reanalysis with a 60-km AGCM and surface pressure observations: OCADA. *J. Meteorol. Soc. Jpn.* **102**, 209–240 (2024).
65. Compo, G. P. et al. The Twentieth Century reanalysis project. *Q. J. R. Meteorol. Soc.* **137**, 1–28 (2011).
66. Zhou, S., Miller, A. J., Wang, J. & Angell, J. K. Trends of NAO and AO and their associations with stratospheric processes. *Geophys. Res. Lett.* **28**, 4107–4110 (2001).
67. Bey, I. et al. Global modeling of tropospheric chemistry with assimilated meteorology: Model description and evaluation. *J. Geophys. Res. Atmos.* **106**, 23073–23095 (2001).
68. Hattori, S. et al. Isotopic evidence for acidity-driven enhancement of sulfate formation after SO_2 emission control. *Sci. Adv.* **7**, eabd4610 (2021).
69. Meinshausen, M. et al. Historical greenhouse gas concentrations for climate modelling (CMIP6). *Geosci. Model Dev.* **10**, 2057–2116 (2017).
70. Liu, H., Jacob, D. J., Bey, I. & Yantosca, R. M. Constraints from 210Pb and 7Be on wet deposition and transport in a global three-dimensional chemical tracer model driven by assimilated meteorological fields. *J. Geophys. Res. Atmos.* **106**, 12109–12128 (2001).
71. Wesely, M. L. Parameterization of surface resistances to gaseous dry deposition in regional-scale numerical models. *Atmos. Environ.* **23**, 1293–1304 (1989).
72. Wang, Y., Jacob, D. J. & Logan, J. A. Global simulation of tropospheric O3-NO -hydrocarbon chemistry: 1. Model formulation. *J. Geophys. Res. Atmos.* **103**, 10713–10725 (1998).
73. Fischer, E. V. et al. Atmospheric peroxyacetyl nitrate (PAN): a global budget and source attribution. *Atmos. Chem. Phys.* **14**, 2679–2698 (2014).
74. Song, S. et al. Fine-particle pH for Beijing winter haze as inferred from different thermodynamic equilibrium models. *Atmos. Chem. Phys.* **18**, 7423–7438 (2018).
75. Wang, X. et al. The role of chlorine in global tropospheric chemistry. *Atmos. Chem. Phys.* **19**, 3981–4003 (2019).
76. Iizuka, Y. et al. Raw and figure data for the manuscript "Acidity-driven gas-particle partitioning of nitrate regulates its transport to Arctic through the industrial era". figshare. Dataset. https://doi.org/10.6084/m9.figshare.25941562 (2025).

Acknowledgements

The authors appreciate to the SE-Dome Ice Core Project members. We are especially grateful to Mr. Tetsuhide Yamasaki and Mr. Morihiro Miyahara, who greatly contributed to the drilling of the ice core and later passed away. The authors acknowledge Ms. Kyoko Gotoda for the ion analysis. The authors would like to thank Becky Alexander and Shuting Zhai for their valuable discussions, including the calculation methods for aerosol pH. This study was supported by MEXT/JSPS KAKENHI Grant Number 23H00511 and 23K18516 (and previous project numbers 18H05292 and 26257201) and the Arctic Challenge for Sustainability (ArCS II) Project, Programme Grant Number JPMXD1420318865. S.I. was supported by MEXT/JSPS KAKENHI Grant 23H03522. S.H. was supported by the National Science Foundation of China (Grant No. W2441015, 42494851, 42494852, and 42473011), MEXT/JSPS KAKENHI [Grant no. 20H04305], the Fundamental Research Funds for the Central Universities [0206/14380918, 0206/143802024, 0206/14380150, 0206/14380185, 0206/14380174, 0206/14380232, International Collaboration Program (Grant no. 2024300346, 0206/14380918)] and Cemac "GeoX" Interdisciplinary Program [Grant no. 2024300245], and startup funding from Nanjing University. S.H. and S.I. were supported by the cooperative research program of the Institute of Nature and Environmental Technology, Kanazawa University (24006). H.M. was supported by MEXT/JSPS KAKENHI Grant Numbers JP23K18519 and JP23K24976. H.M. and N.O. were supported by the Environment Research and Technology Development Fund 2-2301 (JPMEERF20232001) of the Environmental Restoration and Conservation Agency, provided by the Ministry of the Environment of Japan.

Author contributions

Y.I. and S.M. planned this study and conducted the SE-Dome ice core project administration. Y.I., M.M., K.K., M.S. and S.M. contributed to the measurement of ion concentrations. S.I. and S.H. conducted GEOS-Chem model simulations. Y.I., S.I., S.H. and S.M. conducted the data analyses. Y.I. S.I. and S.H. wrote the manuscript. Y.I. S.I. and K.F. prepared figures. Y.I., S.I., S.H., H.M., N.O. and S.M. acquired the funding. R.U., H.M., K.F., N.O., A. Spolaor, A. Svensson, B.M.V., H.O., O.S. and S.M. interpreted the results and provided comments on the manuscript. Y.I., S.I., and S.H. contributed equally to this work.

Competing interests

The authors declare no competing interests.

Additional information

Supplementary information The online version contains supplementary material available at https://doi.org/10.1038/s41467-025-59208-0.

Correspondence and requests for materials should be addressed to Yoshinori Iizuka, Sakiko Ishino or Shohei Hattori.

Peer review information *Nature Communications* thanks Meredith Hastings and the other anonymous reviewer(s) for their contribution to the peer review of this work. A peer review file is available.